Electron-Phonon Interaction Mediated Gigantic Enhancement of Thermoelectric Power Factor Induced by Topological Phase Transition

Zhi Li,[†] Koushik Pal,[‡] Huiju Lee,[¶] Chris Wolverton,*,[†] and Yi Xia*,[¶]

†Department of Materials Science and Engineering, Northwestern University, Evanston, IL 60208, USA

‡Department of Physics, Indian Institute of Technology Kanpur, Kanpur, UP 208016, India

¶Department of Mechanical and Materials Engineering, Portland State University,

Portland, OR 97201, USA

E-mail: c-wolverton@northwestern.edu; yxia@pdx.edu

Abstract

We propose an effective strategy to significantly enhance the thermoelectric power factor (PF) of a series of 2D semimetals and semiconductors by driving them towards a topological phase transition (TPT). Employing first-principles calculations with explicit consideration of electron-phonon interactions, we analyze the electronic transport properties of germanene across the TPT by applying hydrogenation and biaxial strain. We reveal that the nontrivial semimetal phase, hydrogenated germanene with 8% biaxial strain, achieves a considerable fourfold PF enhancement, attributed to the highly asymmetric electronic structure and semimetallic nature of the nontrivial phase. We extend the strategy to another two representative 2D materials—stanene and HgSe—and observe a similar trend, with a marked sixfold and fivefold increase in PF, respectively. The wide selection of functional groups, universal applicability of biaxial strain,

and broad spectrum of 2D semimetals and semiconductors render our approach highly promising for designing novel 2D materials with superior thermoelectric performance.

Thermoelectric (TE) materials, enabling direct heat and electricity conversion, have been intensively studied over the past decades. Their realization affords wide potential applications ranging from waste-heat recycling to microscale cooling. 1,2 To promote the massive application of TE materials, the central challenge is achieving high TE conversion efficiency characterized by the figure of merit $ZT = \sigma S^2 T/\kappa$. Here, σ , S, T, and κ represent the electrical conductivity, Seebeck coefficient, absolute temperature, and thermal conductivity, respectively. Recent advancements in materials sciences and nanotechnology have been considerably pushing the frontiers of TE research . Notably, nanostructured bulk TE materials with thermal conductivity pushed towards the amorphous limit have yielded remarkable ZT reaching approximately 2, $^{9-12}$ equivalent to a Carnot efficiency of about 20%. The consensus is that further improvement in ZT must come from optimizing the electronic transport properties σS^2 , namely, the power factor (PF). Innovative materials design strategies like band convergence, 15,16 resonant levels, 17,18 and modulation doping 19,20 have been proposed to resolve this conundrum in conventional TE materials. However, it is still challenging to enhance PF by several folds through band engineering alone.

Fu et al., ¹⁴ in their recent review, highlight the nontrivial electronic topology in topological materials and their vast potentials for gigantically enhancing PF. Among these materials, topological insulators/semiconductors have garnered extensive attention, owing to intrinsically high PF^{21,22} and the suitability for novel PF enhancement strategies, such as the convergence of regular bands with anisotropic bands²³ or 2D Dirac bands²⁴ and energy filtering effect. ²⁵ Topological semimetals, such as Dirac and Weyl semimetals, though possessing high σ attributed to massless linear bands, are rarely considered for TE applications due to their negligible S resulting from severe bipolar effects. Remarkably, our prior studies have theoretically demonstrated that an energy filtering effect derived from intrinsic electron-phonon interactions (EPI) leads to exceptionally high S in semimetals such as CoSi²⁶ (PF = 76).

 $\mu \mathrm{W/cm/K^2}$ at 300 K) and $\mathrm{MoS_2}^{27}$ (PF = 37 $\mu \mathrm{W/cm/K^2}$ at 300 K). Nevertheless, this effect requires an asymmetric electronic structure featuring a heavy-effective-mass band crossing with linear bands around the Fermi level (E_f), a characteristic not commonly found in most semimetals. Recently, Chen et al.'s work²⁸ on the enhancement of PbSe TE performance towards a topological phase transition (TPT) by external pressure demonstrates the possibility of fine-tuning the topological states. The topology-mandated band inversion at the Dirac point during TPT guarantees the emergence of aforementioned band-crossing features, which promises for gigantic PF enhancement in trivial semimetals and semiconductors. Given the stronger correlation between electronic topology and transport in 2D materials due to the inherent quantum confinement effect, ²⁹ they stand out as superior candidates for implementing the strategy and exemplifying its influence. Moreover, recent studies have demonstrated the flexibility of applying multiple approaches, including external electric field, ³⁰ biaxial strain ³¹, and functionalization, ³² for modifying the electronic structure in 2D materials, providing practical ways to induce TPT in these systems.

In this Letter, we propose an effective strategy to significantly enhance PF via inducing TPT by hydrogenation and application of biaxial strain in a series of 2D monolayer compounds, including germanene, stanene, and HgSe. Employing rigorous first-principles calculations with an explicit consideration of EPI, we thoroughly analyzed the electronic properties of these materials across the TPT. We uncover the underlying mechanism that significantly enhances PF in the topological nontrivial semimetal phase. The versatility of our strategy promises applicability to a broad spectrum of 2D materials, including both their semimetal and semiconductor phases.

Germanene is in hexagonal honeycomb structure (Figure 1a) with a calculated lattice parameter a=4.05 Å, in good agreement with previous studies.^{33,34} As depicted in Figure 1c, the in-plane orbitals of Ge, i.e. 4s, $4p_x$, and $4p_y$, hybridize to form covalent bonds, manifesting as a light conduction band, along with a light and a heavy valence bands nesting at the Γ point. Meanwhile, the out-of-plane orbitals, $4p_z$, contribute to π -bonds, resulting in

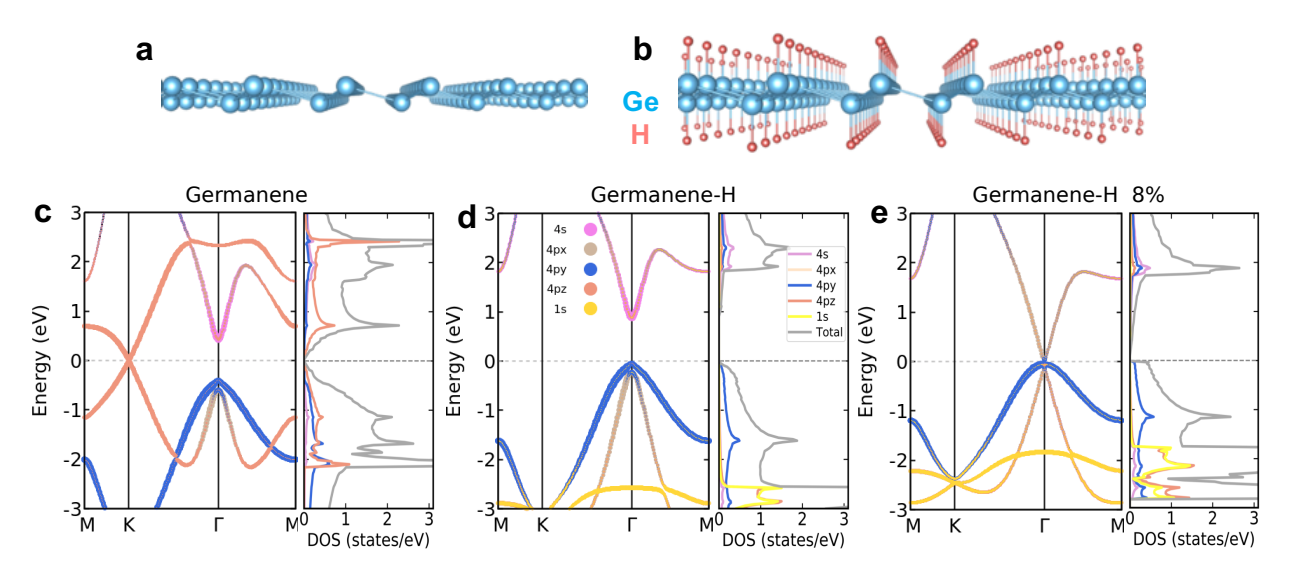


Figure 1: Perspective views of (a) germanene and (b) hydrogenated germanene (GeH) wherein hydrogen and germanium atoms colored red and blue, respectively. Orbital-resolved electronic structures and density of states (DOS) of (c) germanene, (d) GeH, and (e) GeH applied with a critical biaxial strain of 8% (GeH-8%), respectively. Spin-orbit coupling (SOC) effects were included in the calculation of electronic structures.

a massless Dirac band at the K point. With the spin-orbit coupling (SOC) effect included in our calculations, a negligible SOC bandgap of 28 meV opens up at the K point, consistent with previous findings. 34,35 When E_f situated at the Dirac point, the Dirac band dominates the electronic transport and leads to a high carrier mobility, presenting a typical semimetallic character. This typical semimetal phase exhibits inferior PF due to the low S arising from severe bipolar effect. Consequently, we seek to modify the electronic topology of germanene by TPT and induce asymmetric band-crossing feature, which promises for significantly enhancing PF. Previous studies $^{36-39}$ have shown that the electronic structure of germanene can be modified by biaxial strains and functionalization. These modified forms of germanene exhibit various topological phases, including trivial semiconductors, nontrivial semimetals, and nontrivial insulators. These findings indicate the potential for TPT during the evolution of germanene's electronic topology. Notably, though many functional groups, such as H, OH, F, CH₃, etc., $^{37,40-42}$ were explored theoretically, only the hydrogenated germanene, i.e. GeH, was experimentally synthesized. 43 This highlights our motivation to further investigate the

potential TPT in GeH. In GeH (Figure 1b), the formation of σ -bonds between Ge and H removes the Dirac band at K point (Figure 1d). This leads to the proximity of in-plane bonding states to E_f , enabling the semiconducting nature of GeH with a bandgap of 1.03 eV. Further application of biaxial strain on the GeH lattice decreases the bandgap at the Γ point. Eventually, with 8% of the biaxial strain applied, GeH goes through TPT and exhibits the desired asymmetric band-crossing feature — the light valence band and conduction band merge into a linear band, crossing with the heavy valence band at the Γ point (Figure 1e). Comparative analysis of GeH band structures with or without SOC (detailed in Supporting Information) indicates the critical band-crossing feature persists under both conditions, consistent with Ren et al.'s 42 recent study of GeH. We emphasize that SOC is necessary for the TPT, as confirmed by previous studies. 41,42,44 However, the essence of our strategy—the asymmetric band crossing at E_f —varies negligibly with the SOC effect. Consequently, the relative enhancement of PF due to this feature should remain consistent under both SOC and non-SOC frameworks. Given the substantial increase of computational cost when considering the SOC effect in EPI, we exclude it in the following electronic transport calculations.

We now move on to discuss the impacts of TPT-induced asymmetric band crossing on thermoelectric properties, including S, σ , and PF. Figure 2a shows the calculated S as a function of reduced chemical potential (μ -E_f) for germanene and GeH with application of various biaxial strains (GeH-4/6/8%). Near the valence band maximum (VBM) or conduction band minimum (CBM), GeH-4% and GeH-6% present very large S, aligning with the semiconducting nature of the two phases which possess a finite bandgap. In contrast, much smaller S are observed for the other two semimetal phases, germanene and GeH-8%, consistent with their semimetallic nature with strong bipolar effects. However, distinctive features in S, including both magnitudes and symmetries, are found between germanene and GeH-8%. The S of germanene exhibits symmetric behavior near E_f , whereas the GeH-8% displays rather asymmetric behavior that shows much larger peak value of negative S when

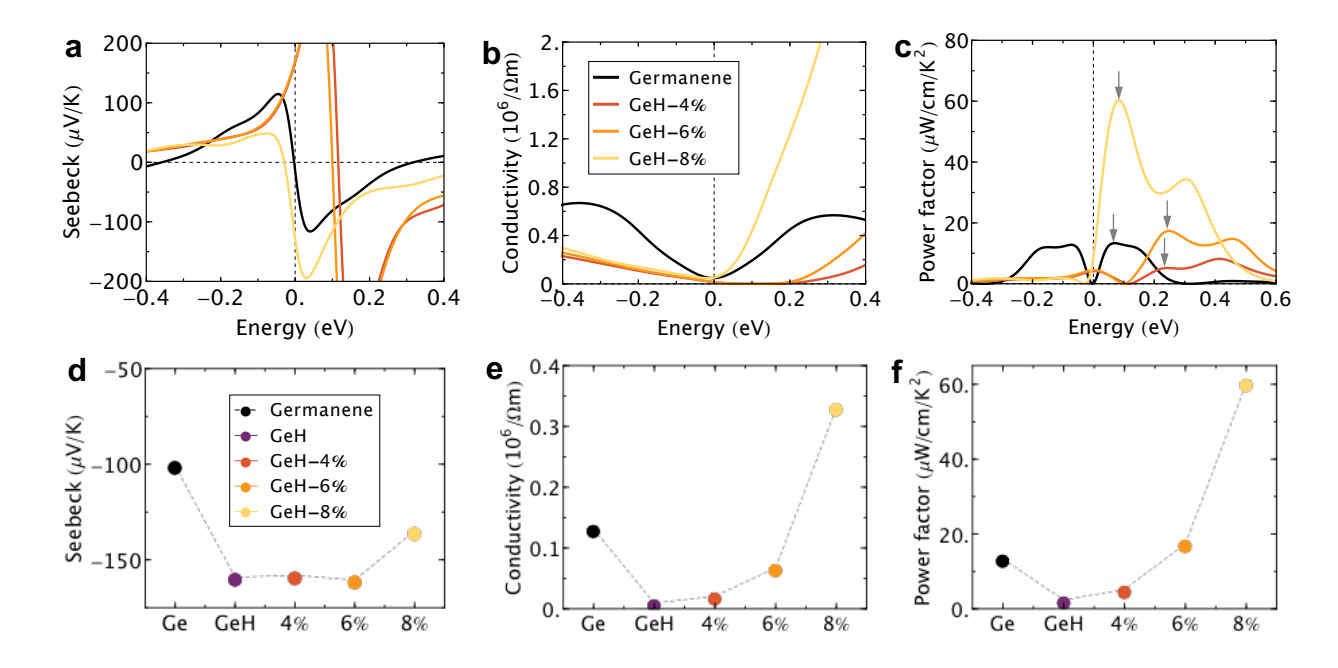


Figure 2: Thermoelectric transport properties of germanene and hydrogenated germanene (GeH) with application of various biaxial strains (GeH-4/6/8%). Theoretically calculated (a) Seebeck coefficient, (b) electrical conductivity, and (c) power factor (PF) as a function of reduced chemical potential (μ -E_f). (d)-(f) displays the values of Seebeck coefficient, electrical conductivity, and power factor at the reduced chemical potential that leads to the optimal power factor (first peak away from the E_f) in germanene, GeH, and GeH-4/6/8%, respectively. The gray dashed lines are guides to the eye.

the chemical potential moves to slightly above E_f . Such vastly contrasting behaviors in the two semimetal phases might be traced back to the presence of the heavy band near the Dirac point in GeH-8%. A similar asymmetric behavior of GeH-8% can be seen in the calculated chemical-potential-dependent σ as shown in Figure 2b. The conductivity above E_f attains a significantly higher value than that below E_f , indicating a non-negligible difference in the transport of holes and electrons in GeH-8%. Meanwhile, σ is generally much larger in the two semimetal phases than the two semiconductor phases, which is not unexpected since σ are significantly boosted with the presence of massless Dirac bands which possess larger Fermi velocities. As displayed in Figure 2c, the PF shows a drastic change from germanene to GeH-8% and the latter retains the largest magnitude in a vast chemical potential range above E_f , as well as the strongest asymmetric behavior across E_f . To elucidate the enhancement in PF as the electronic structure transitions from germanene to GeH, GeH-4/6%, and GeH-8%, we show S and σ in Figures 2d and 2e, respectively. These values are associated with the peak PF values closest to E_f (Figure 2f) for the respective systems, as marked by arrows in Figure 2c. Figures 2d suggests that S associated with the optimal PF display very similar values ($\approx 160 \ \mu V/K$) in the semiconductor phases (GeH and GeH-4/6%), while GeH-8% has a value of about -135 μ V/K which is about 35% larger than that of germanene (\sim -100 $\mu V/K$). Concerning the conductivity, it is significantly reduced from germanene to GeH and then increases as the finite bandgap deminishing, reaching a maximum value in GeH-8% (Figure 2e). Figure 2f shows that the optimal PF exhibit similar trends as σ . Therefore, it can be inferred that the maximum PF achieved in GeH-8% results from maintaining a fairly large S while achieving a gigantic enhancement in σ .

Despite the strong correlation with the sharp change in the electronic structure, the physical mechanism underlying the peculiar enhancement in PF cannot be attributed to static band structure properties alone. It is essential to consider the dynamic processes, namely, the specific scattering processes arising from EPI. This conclusion is inferred from a control calculation that employs the constant relaxation time approximation (CRTA). Without

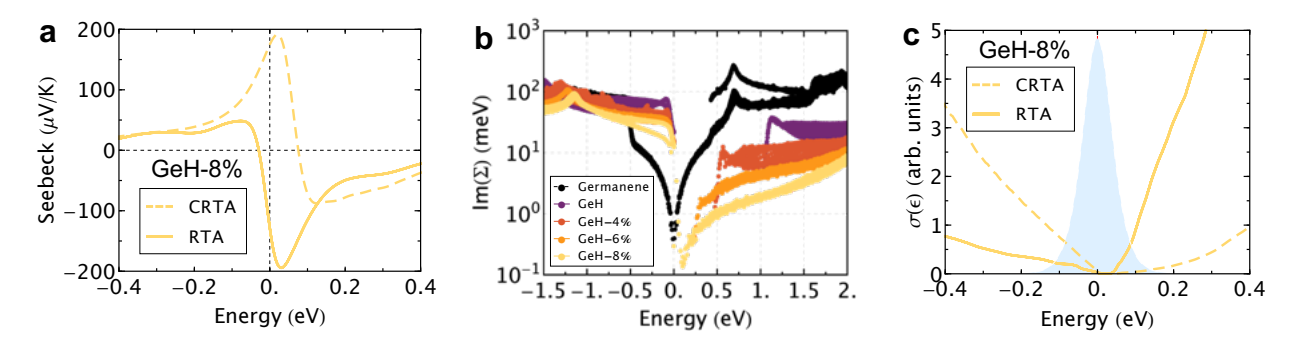


Figure 3: (a) Calculated Seebeck coefficient as a function of reduced chemical potential at 300 K in semimetal GeH-8% using the constant relaxation time approximation (CRTA) and relaxation time approximation (RTA). (b) Calculated energy-dependent imaginary part of electron self-energy of germanene, hydrogenated germanene (GeH), and GeH applied with various biaxial strains (GeH-4/6/8%) at 300 K. (c) The same as (a) but for the transport distribution function $\sigma(\epsilon)$. Blue shade indicates the energy range of major carriers that obey Fermi-Dirac distribution.

considering the variation of electron lifetime, ⁴⁵ the CRTA fails drastically in computing S of GeH-8%. As shown in Figure 3a, a notable discrepancy of S is found near the E_f . At the E_f , the CRTA predicts a S of 175 μ V/K, while RTA yields -141 μ V/K, indicating a radical sign change induced by EPI. To elucidate the underlying mechanisms, we analyze S using the Mott formula ⁴⁶ within the degenerate limit (μ = $E_f\pm k_BT$, note this only serves as a conceptual demonstration rather than the exact formula used for calculating S in this study, see details in **Supporting Information**)

$$S = -\frac{\pi^2 k_{\rm B}^2 T}{3e} \left. \frac{d \ln \sigma(\epsilon)}{d\epsilon} \right|_{\epsilon=\mu},\tag{1}$$

where $\sigma(\epsilon) = n(\epsilon)v^2(\epsilon)\tau(\epsilon)e$ is termed the transport distribution function, ⁴⁷ and e, $n(\epsilon)$, $v(\epsilon)$ and $\tau(\epsilon)$ are the absolute charge of an electron, enegy-dependent density of states, Fermi velocity, and lifetime, respectively. The Mott formula essentially reveals that S is proportional to the negative of the energy derivative of $\sigma(\epsilon)$. When CRTA is employed (Figure 3c), an abrupt reduction of $\sigma(\epsilon)$ in GeH-8% is observed when the chemical potential shifts upward away from the heavy band, giving rise to a large negative derivative of $\sigma(\epsilon)$ and thus large positive S near the E_f . By contrast, the large negative S under RTA unambiguously

reveals a strong energy dependence of lifetime $\tau(\epsilon)$ (omitted by CRTA) near the E_f , which not only changes the sign of S but also ensures its large absolute magnitude. Indeed, it is confirmed in Figure 3b, wherein the energy-dependent imaginary part of electron self-energy $(1/\tau \propto \text{Im}(\Sigma))$ arising from the intrinsic EPI is explicitly depicted. The results clearly reveal that the abrupt decrease in $\text{Im}(\Sigma)$ (increase in $\tau(\epsilon)$) near the E_f becomes stronger and stronger across the TPT from germanene to GeH-8%. The largest change is found in GeH-8% which shows increased $\tau(\epsilon)$ by more than two orders of magnitude across the E_f . When this abrupt lifetime change is considered, the transport distribution function $\sigma(\epsilon)$ is drastically modified. As detailed in Figure 3c, $\sigma(\epsilon)$ under RTA increases sharply across the E_f , giving rise to large negative S.

The pronounced variation in lifetimes near the E_f not only affects S but also σ . The exceptionally long lifetimes associated with the linear bands above the E_f in GeH-8%, combined with the large Fermi velocity, leads to remarkable conductivity across a wide range of chemical potentials (Figure 2b). To understand the peculiarities of lifetimes, an examination of the details of electron-phonon scattering is necessary. We select three phases across the TPT—germanene, GeH, and GeH-8%—to demonstrate the distinct electron-phonon scattering process. Figure 4a reveals that the acoustic (PMG1) and optical phonon (PMG2) branches in germanene are well separated by a finite phononic bandgap. The major difference in phonon dispersions among these three phases are the additional six optical branches in GeH and GeH-8%. These optical branches all have energy higher than 50 meV, forming two well separated groups (Figures 4b and 4c), which corresponds to the bending (PMG3) and stretching of Ge-H bonds (PMG4). Notably, due to the polar and semiconducting nature of GeH phase, there are polar optical phonon modes (in PMG3) which gives rise to a finite slope of phonon energies at the zone center, 48 potentially introducing extra scattering for electrons. Contributions to $\text{Im}(\Sigma)$ from each phonon mode groups are shown in Figures 4d-4f. Compared to germanene (Figure 4d), GeH shows asymmetric $\operatorname{Im}(\Sigma)$ across the E_f , with dominant contribution from PMG3 (Figure 4e). A more asymmetric $Im(\Sigma)$ is observed in

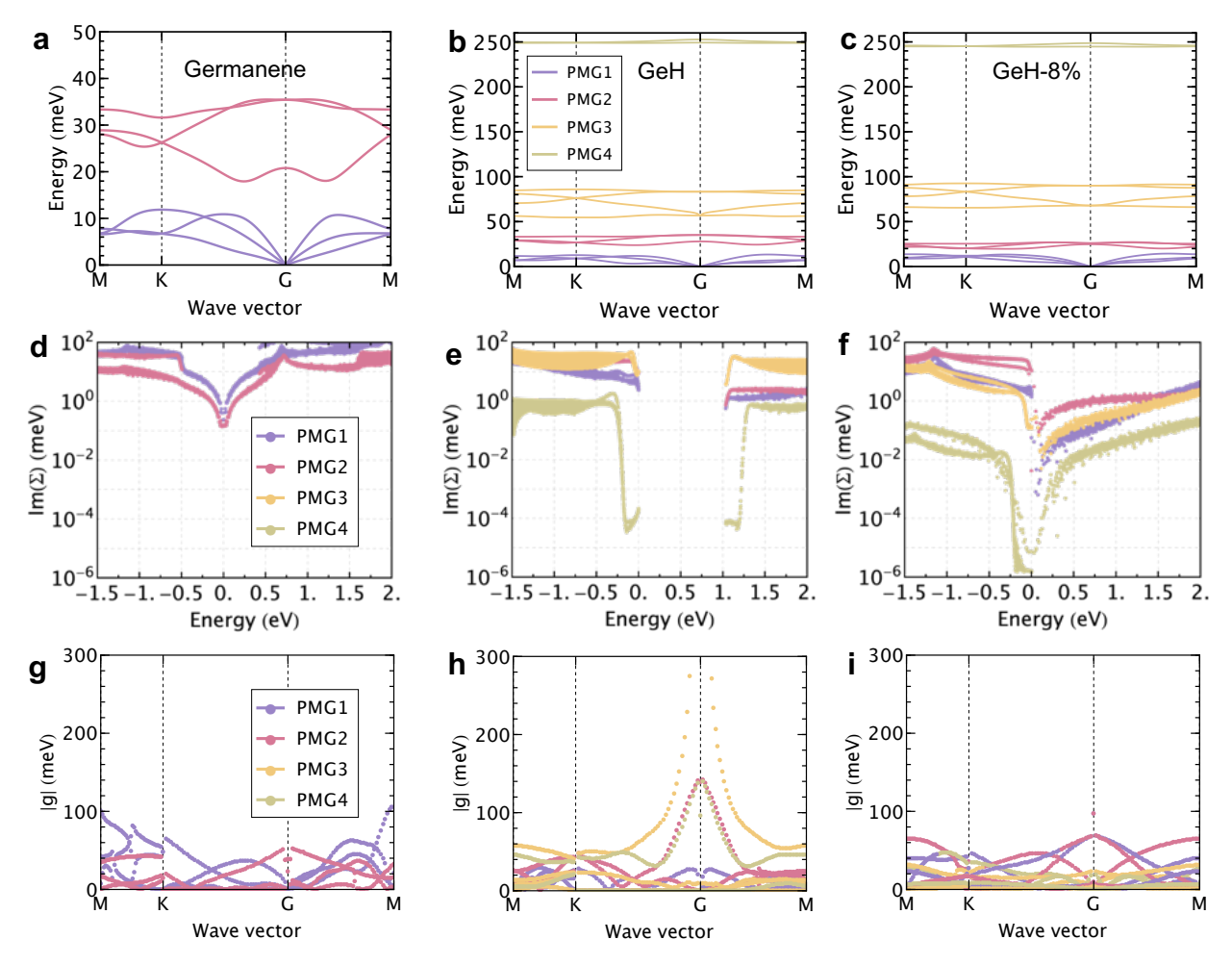


Figure 4: (a)-(c) Calculated phonon dispersions of germanene, hydrogenated germanene (GeH) and GeH under 8% biaxial strain (GeH-8%), respectively. Phonon branches are grouped into four phonon mode groups (PMG) with different colors. PMG1 indicates the low-lying three acoustic branches, PMG2 indicates the low-lying three optical branches, PMG3 denotes the intermediate four optical branches including the polar optical branch, and PMG4 shows the high-lying tow optical branches. (d)-(f) Calculated energy-dependent imaginary part of electron self-energy $Im(\Sigma)$ at 300 K of germanene, GeH, and GeH-8%, respectively. $Im(\Sigma)$ is further decomposed into contributions from the electron-phonon interactions arising from the four phonon mode groups as defined above. (g)-(i) Electron-phonon interaction matrix element |g| along the high symmetry points of the irreducible Brillouin zone. These matrix elements, which are colored according to the four phonon mode groups defined above, denote the scattering strength of the electronic states at the valence band maximum (VBM) by phonon modes with various frequencies and wave vectors.

GeH-8% (Figure 4f), while contribution from PMG3 is significantly suppressed. These distinctions can be ultimately traced back to the key ingredients entering the expression of $Im(\Sigma)$, as described below:

$$\operatorname{Im}(\Sigma) = \pi \sum_{j,v} \int_{BZ} \frac{d\mathbf{q}}{\Omega_{BZ}} |g_{ji,v}(\mathbf{k}, \mathbf{q})|^{2} \times \left[(n_{v,\mathbf{q}} + f_{j,\mathbf{k}+\mathbf{q}}) \delta\left(\epsilon_{i,\mathbf{k}} + \omega_{v,\mathbf{q}} - \epsilon_{j,\mathbf{k}+\mathbf{q}}\right) + (1 + n_{v,\mathbf{q}} - f_{j,\mathbf{k}+\mathbf{q}}) \delta\left(\epsilon_{i,\mathbf{k}} - \omega_{v,\mathbf{q}} - \epsilon_{j,\mathbf{k}+\mathbf{q}}\right) \right],$$
(2)

where v, \mathbf{q} , ω , n, and $g_{ji,v}(\mathbf{k},\mathbf{q})$ are the phonon mode index, wave vector, frequency, population, and electron-phonon interaction matrix element (denoted as |g| in subsequent discussions). The terms in the brackets represent an electron-phonon scattering phase space Φ allowed by energy and momentum conservation. Disregarding the complexity induced by crystal symmetry, it is apparent that a heavy band (the minimal energy variation across a extensive range of momentum change) provides a larger Φ , which more directly reflects on a higher density of state (DOS, $n(\epsilon)$). As inferred from the above definition, $Im(\Sigma)$ is proportional to $|g|^2$ and $n(\epsilon)$, i.e., $\text{Im}(\Sigma) \propto |g|^2 n(\epsilon)$. Since |g| in germanene and GeH-8% exhibit similar strengths (Figures 4g and 4i), the asymmetric (GeH-8%) and symmetric (germanene) $\operatorname{Im}(\Sigma)$ with respect to E_f as well as the their magnitudes can be mostly attributed to the DOS. This argument also applies to $Im(\Sigma)$ of GeH from PMG1/PMG2/PMG4. That is, the symmetric massless linear band in germanene leads to a symmetric $\text{Im}(\Sigma)$ with overall low intensity, whereas the presence of a heavy band in GeH leads to an asymmetric $Im(\Sigma)$ showing much higher intensity below the E_f . The coexistence of linear and heavy bands in GeH-8% exhibits a combination of the above features, while presenting the minimal $Im(\Sigma)$ (Figure 3b) due to the decreased DOS. On the other hand, the significantly reduced |q| near the Γ point from PMG3 in GeH-8%, compared to GeH, is attributed to its semimetallic nature with non-polar optical phonons. Therefore, it is conclusive that the significant reduction in $\text{Im}(\Sigma)$ when semiconducting GeH is strained into semimetallic GeH-8% results from (i) a decrease in DOS due to the energy filtering effect and (ii) a decrease in |g| due to the elimination of polar optical phonon scattering. In addition, though DOS decreased, the higher conductivity of linear band above the E_f in GeH-8% compared to that of germanene (Figure 2b) also highlights the importance of lifetime effects which may dominate over the DOS effects in contributing to high conductivity.⁴⁹

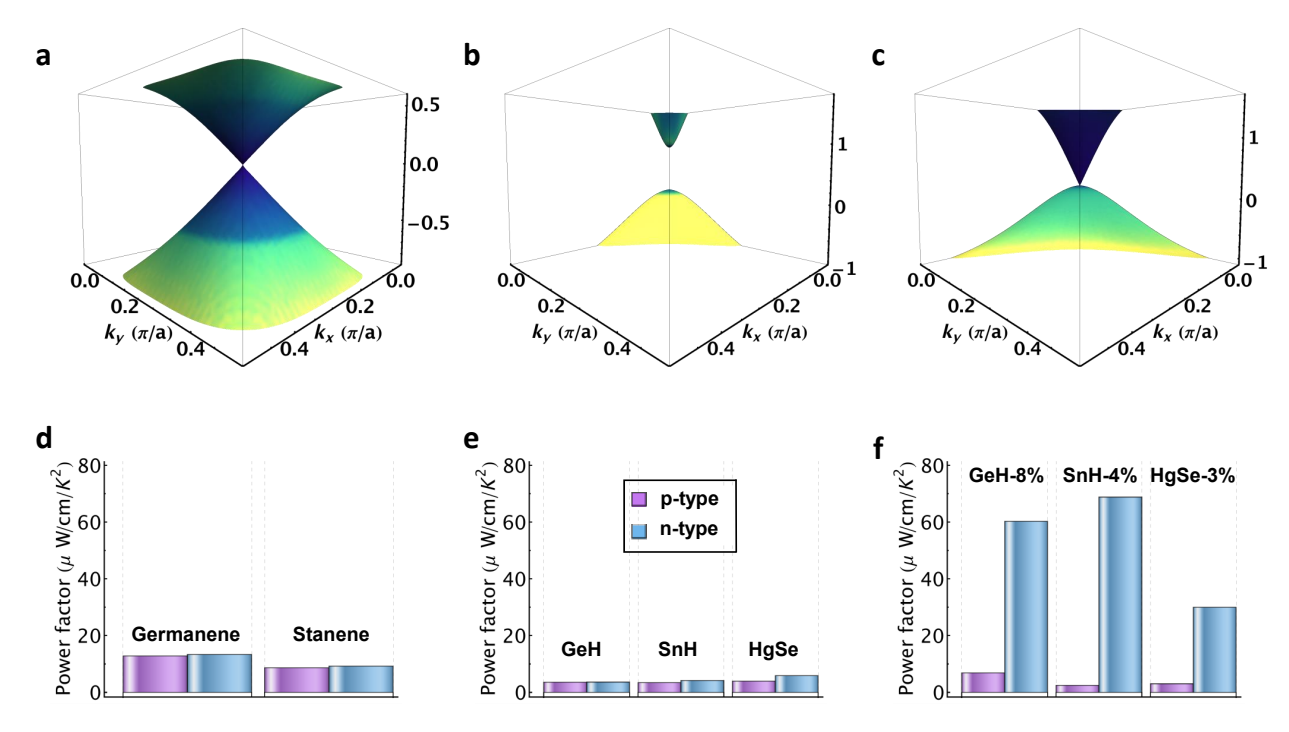


Figure 5: (a)-(c) Schematic plot of the electronic structure evolution towards the topological phase transition from (a) typical nontrivial semimetal to (b) trivial semiconductor to (c) atypical nontrivial semimetal. The band structures are colored according to the magnitudes of imaginary part of electron self-energy $\operatorname{Im}(\Sigma)$ with blue indicating small values while yellow large values. (d)-(f) Calculated optimal thermoelectric power factor of both p- and n-type monolayer germanene, stanene, their hydrogenated counterparts and HgSe with and without strain at 300 K.

The essential features relevant to aforementioned enhancement are elucidated in the evolution of the electronic structure and dynamics, transitioning from typical nontrivial semimetal germanene to trivial semiconductor GeH, and ultimately to atypical nontrivial semimetal GeH-8%, as shown in Figures 5 a-5 c. In the case of germanene (Figure 5a), electronic states near the E_f are symmetric and exhibiting small $Im(\Sigma)$, resulting in appreciable

 σ but minimal S. When a finite bandgap opens in the case of GeH (Figure 5b), $\text{Im}(\Sigma)$ is significantly enhanced at both the VBM and CBM. Despite the substantial S due to the presence of bandgap, σ is markedly suppressed by the polar optical phonon scattering. By straining the semicondutor GeH into a nontrivial semimetal topological phase (Figure 5c), $\operatorname{Im}(\Sigma)$ is significantly reduced at conduction bands while preserving strong asymmetry between conduction and valence bands. This asymmetry fosters a large S arising from the filtering of low-energy holes by the presence of a heavy valence band. Combined with the ultrahigh σ guaranteed by the bare linear bands, a gigantic enhancement of PF is realized in GeH-8%. This suggests constructing a band structure comprising both a massless linear band and a heavy band crossing at the E_f is particularly advantageous for achieving a high PF. To extend this strategy to more systems, similar calculations were performed for another group-IV 2D material, stanene (detailed in **Supporting Information**). We have found the bare linear bands inherent in stanene give rise to an optimal PF of less than 10 μ W/cm/K² (Figure 5d). In contrast, when stanene is hydrogenated and under a critical strain of 4%, the optimal PF achieves a remarkable enhancement to 70 μ W/cm/K² (Figure 5f), over sevenfold that of pristine stanene. Moreover, we explore cases beyond the group-IV 2D materials using the semiconductor HgSe monolayer (detailed in **Supporting Information**). It has been demonstrated by Li et al. 50 that monolayer low-buckled HgSe undergoes a similar TPT with the evolution of electronic band structure under strain of about 3%. The calculated optimal PF of the nontrivial semimetal phase HgSe achieved a remarkable enhancement of about fivefold. We emphasize that the major achievement here is the demonstration of relative enhancement of PF rather than absolute values which might be sensitive to the level of theory used such as relaxation time approximation, rigid band approximation, and SOC effects. 51-54

To summarize, we proposed an effective strategy to significantly enhance the PF. By applying a combined modification of functionalization and biaxial strain, we theoretically induce the TPT in a series of 2D materials, including germanene, stanene, and HgSe mono-

layer. Our investigation involves rigorous first-principles calculations considering both the static electronic structure and the dynamic EPI. We revealed that a massless linear band crossing with a heavy band at the E_f can create significant change in carrier lifetime by selectively scattering one type of carriers, which results in substantial enhancements in S that is not commonly seen in typical semimetal phases. Meanwhile, the decrease in DOS and elimination of polar optical phonon scattering in strained semimetal phases also accounted for a significant enhancement in σ . A well-balanced interplay between S and σ eventually contributed to a gigantically enhanced PF, which is promising for high-performance 2D thermoelectric materials. Our findings pave the way for the design and optimization of 2D thermoelectric materials, suggesting that a combination of functionalization and biaxial strain could be a key strategy for constructing the critical asymmetric band-crossing feature, which is rarely seen in the trivial semimetals and semiconductors.

Acknowledgement

This work is partially supported by the U.S. Department of Energy, Office of Science Basic Energy Sciences under grant DE-SC0024256. We acknowledge the computing resources provided by Bridges2 at Pittsburgh Supercomputing Center (PSC) through allocations dmr160112, dmr160027p, mat220006p, and mat220008p from the Advanced Cyberinfrastructure Coordination Ecosystem: Services & Support (ACCESS) program, which is supported by National Science Foundation grants #2138259, #2138286, #2138307, #2137603, and #2138296. Y. X. acknowledges support from the US National Science Foundation through award #2317008. H. L. was supported by the MOTIE (Ministry of Trade, Industry, and Energy) in Korea, under the Fostering Global Talents for Innovative Growth Program (P0008750) supervised by the Korea Institute for Advancement of Technology (KIAT). Z. L. and C. W. acknowledge the support from the Center for Hierarchical Materials Design (CHiMaD) under the award 70NANB14H012 by U.S. Department of Commerce and compu-

tational resource from the National Energy Research Scientific Computing Center (NERSC) through allocation m4545.

References

- (1) Pourkiaei, S. M.; Ahmadi, M. H.; Sadeghzadeh, M.; Moosavi, S.; Pourfayaz, F.; Chen, L.; Yazdi, M. A. P.; Kumar, R. Thermoelectric cooler and thermoelectric generator devices: A review of present and potential applications, modeling and materials. Energy 2019, 186, 115849.
- (2) Shi, X.-L.; Zou, J.; Chen, Z.-G. Advanced thermoelectric design: from materials and structures to devices. *Chemical Reviews* **2020**, *120*, 7399–7515.
- (3) Venkatasubramanian, R.; Siivola, E.; Colpitts, T.; O'quinn, B. Thin-film thermoelectric devices with high room-temperature figures of merit. *Nature* **2001**, *413*, 597–602.
- (4) Yoshida, M.; Iizuka, T.; Saito, Y.; Onga, M.; Suzuki, R.; Zhang, Y.; Iwasa, Y.; Shimizu, S. Gate-optimized thermoelectric power factor in ultrathin WSe2 single crystals. *Nano letters* 2016, 16, 2061–2065.
- (5) Duan, J.; Wang, X.; Lai, X.; Li, G.; Watanabe, K.; Taniguchi, T.; Zebarjadi, M.; Andrei, E. Y. High thermoelectricpower factor in graphene/hBN devices. *Proceedings* of the National Academy of Sciences 2016, 113, 14272–14276.
- (6) Flores, E.; Ares, J. R.; Castellanos-Gomez, A.; Barawi, M.; Ferrer, I. J.; Sánchez, C. Thermoelectric power of bulk black-phosphorus. *Applied Physics Letters* **2015**, *106*.
- (7) Xie, H.; Bozin, E. S.; Li, Z.; Abeykoon, M.; Banerjee, S.; Male, J. P.; Snyder, G. J.; Wolverton, C.; Billinge, S. J.; Kanatzidis, M. G. Hidden Local Symmetry Breaking in Silver Diamondoid Compounds is Root Cause of Ultralow Thermal Conductivity. Advanced Materials 2022, 34, 2202255.

- (8) Liu, D.; Wang, D.; Hong, T.; Wang, Z.; Wang, Y.; Qin, Y.; Su, L.; Yang, T.; Gao, X.; Ge, Z., et al. Lattice plainification advances highly effective SnSe crystalline thermoelectrics. *Science* **2023**, *380*, 841–846.
- (9) Zhang, Y.; Li, Z.; Singh, S.; Nozariasbmarz, A.; Li, W.; Genç, A.; Xia, Y.; Zheng, L.; Lee, S. H.; Karan, S. K., et al. Defect-Engineering-Stabilized AgSbTe2 with High Thermoelectric Performance. *Advanced Materials* **2023**, *35*, 2208994.
- (10) Xing, T.; Zhu, C.; Song, Q.; Huang, H.; Xiao, J.; Ren, D.; Shi, M.; Qiu, P.; Shi, X.; Xu, F., et al. Ultralow lattice thermal conductivity and superhigh thermoelectric figure-of-merit in (Mg, Bi) co-doped GeTe. Advanced Materials 2021, 33, 2008773.
- (11) Zhang, Q.; Ti, Z.; Zhu, Y.; Zhang, Y.; Cao, Y.; Li, S.; Wang, M.; Li, D.; Zou, B.; Hou, Y., et al. Achieving ultralow lattice thermal conductivity and high thermoelectric performance in GeTe alloys via introducing Cu2Te nanocrystals and resonant level doping. ACS nano 2021, 15, 19345–19356.
- (12) Liu, Y.; Xie, H.; Li, Z.; Zhang, Y.; Malliakas, C. D.; Al Malki, M.; Ribet, S.; Hao, S.; Pham, T.; Wang, Y., et al. Unraveling the Role of Entropy in Thermoelectrics: Entropy-Stabilized Quintuple Rock Salt PbGeSnCd x Te3+ x. Journal of the American Chemical Society 2023, 145, 8677–8688.
- (13) DiSalvo, F. J. Thermoelectric cooling and power generation. *Science* **1999**, *285*, 703–706.
- (14) Fu, C.; Sun, Y.; Felser, C. Topological thermoelectrics. APL Materials 2020, 8.
- (15) Li, W.; Zheng, L.; Ge, B.; Lin, S.; Zhang, X.; Chen, Z.; Chang, Y.; Pei, Y. Promoting SnTe as an eco-friendly solution for p-PbTe thermoelectric via band convergence and interstitial defects. *Advanced Materials* **2017**, *29*, 1605887.

- (16) Pathak, R.; Sarkar, D.; Biswas, K. Enhanced Band Convergence and Ultra-Low Thermal Conductivity Lead to High Thermoelectric Performance in SnTe. Angewandte Chemie International Edition 2021, 60, 17686–17692.
- (17) Wu, L.; Li, X.; Wang, S.; Zhang, T.; Yang, J.; Zhang, W.; Chen, L.; Yang, J. Resonant level-induced high thermoelectric response in indium-doped GeTe. *NPG Asia Materials* **2017**, *9*, e343–e343.
- (18) Liu, H.-T.; Sun, Q.; Zhong, Y.; Xia, C.-L.; Chen, Y.; Shi, X.-L.; Chen, Z.-G.; Ang, R. Enhanced thermoelectric performance of n-type Nb-doped PbTe by compensating resonant level and inducing atomic disorder. *Materials Today Physics* **2022**, *24*, 100677.
- (19) Wang, S.-J.; Panhans, M.; Lashkov, I.; Kleemann, H.; Caglieris, F.; Becker-Koch, D.; Vahland, J.; Guo, E.; Huang, S.; Krupskaya, Y., et al. Highly efficient modulation doping: A path toward superior organic thermoelectric devices. *Science Advances* 2022, 8, eabl9264.
- (20) Zheng, J.; Wang, S.; Zhao, Z.; Gao, X.; Hong, T.; Zhao, L.-D. Modulation Doping Leads to Optimized Thermoelectric Properties in n-Type Bi6Cu2Se4O6 due to Interface Effects. Advanced Functional Materials 2023, 2300447.
- (21) Jabar, B.; Qin, X.; Mansoor, A.; Ming, H.; Huang, L.; Danish, M. H.; Zhang, J.; Li, D.; Zhu, C.; Xin, H., et al. Enhanced power factor and thermoelectric performance for n-type Bi2Te2. 7Se0. 3 based composites incorporated with 3D topological insulator nanoinclusions. Nano Energy 2021, 80, 105512.
- (22) Tang, X.; Li, Z.; Liu, W.; Zhang, Q.; Uher, C. A comprehensive review on Bi2Te3-based thin films: thermoelectrics and beyond. *Interdisciplinary Materials* **2022**, *1*, 88–115.
- (23) Li, A.; Hu, C.; He, B.; Yao, M.; Fu, C.; Wang, Y.; Zhao, X.; Felser, C.; Zhu, T. Demonstration of valley anisotropy utilized to enhance the thermoelectric power factor.

 Nature Communications 2021, 12, 5408.

- (24) Pan, Y.; Fan, F.-R.; Hong, X.; He, B.; Le, C.; Schnelle, W.; He, Y.; Imasato, K.; Borrmann, H.; Hess, C., et al. Thermoelectric properties of novel semimetals: A case study of YbMnSb2. *Advanced Materials* **2021**, *33*, 2003168.
- (25) Kommini, A.; Aksamija, Z. Anisotropic thermoelectric power factor of two-dimensional materials with periodic potential barriers: the Wigner-Rode formalism. *Physical Review Applied* **2020**, *14*, 034037.
- (26) Xia, Y.; Park, J.; Zhou, F.; Ozoliņš, V. High Thermoelectric Power Factor in Intermetallic Co Si Arising from Energy Filtering of Electrons by Phonon Scattering. Physical Review Applied 2019, 11, 024017.
- (27) Xia, Y.; Park, J.; Ozoliņš, V.; Wolverton, C. Leveraging electron-phonon interaction to enhance the thermoelectric power factor in graphene-like semimetals. *Physical Review* B 2019, 100, 201401.
- (28) Chen, L.-C.; Chen, P.-Q.; Li, W.-J.; Zhang, Q.; Struzhkin, V. V.; Goncharov, A. F.; Ren, Z.; Chen, X.-J. Enhancement of thermoelectric performance across the topological phase transition in dense lead selenide. *Nature Materials* **2019**, *18*, 1321–1326.
- (29) Hicks, L. D.; Harman, T. C.; Dresselhaus, M. S. Use of quantum-well superlattices to obtain a high figure of merit from nonconventional thermoelectric materials. *Applied Physics Letters* **1993**, *63*, 3230–3232.
- (30) Kuc, A.; Heine, T. The electronic structure calculations of two-dimensional transition-metal dichalcogenides in the presence of external electric and magnetic fields. *Chemical Society Reviews* **2015**, *44*, 2603–2614.
- (31) Yang, S.; Chen, Y.; Jiang, C. Strain engineering of two-dimensional materials: methods, properties, and applications. *InfoMat* **2021**, *3*, 397–420.

- (32) Brill, A. R.; Koren, E.; de Ruiter, G. Molecular functionalization of 2D materials: from atomically planar 2D architectures to off-plane 3D functional materials. *Journal of Materials Chemistry C* **2021**, *9*, 11569–11587.
- (33) Li, L.; Lu, S.-z.; Pan, J.; Qin, Z.; Wang, Y.-q.; Wang, Y.; Cao, G.-y.; Du, S.; Gao, H.-J. Buckled germanene formation on Pt (111). *Advanced Materials* **2014**, *26*, 4820–4824.
- (34) Acun, A.; Zhang, L.; Bampoulis, P.; Farmanbar, M. v.; van Houselt, A.; Rudenko, A.; Lingenfelder, M.; Brocks, G.; Poelsema, B.; Katsnelson, M., et al. Germanene: the germanium analogue of graphene. *Journal of physics: Condensed matter* **2015**, *27*, 443002.
- (35) Liu, N.; Bo, G.; Liu, Y.; Xu, X.; Du, Y.; Dou, S. X. Recent progress on germanene and functionalized germanene: preparation, characterizations, applications, and challenges. Small 2019, 15, 1805147.
- (36) Yan, J.-A.; Gao, S.-P.; Stein, R.; Coard, G. Tuning the electronic structure of silicene and germanene by biaxial strain and electric field. *Physical Review B* **2015**, *91*, 245403.
- (37) Houssa, M.; Scalise, E.; Sankaran, K.; Pourtois, G.; Afanas'Ev, V.; Stesmans, A. Electronic properties of hydrogenated silicene and germanene. *Applied Physics Letters* **2011**, *98*.
- (38) Jing, Y.; Zhang, X.; Wu, D.; Zhao, X.; Zhou, Z. High carrier mobility and pronounced light absorption in methyl-terminated germanene: Insights from first-principles computations. *The Journal of Physical Chemistry Letters* **2015**, *6*, 4252–4258.
- (39) Chandiramouli, R.; Nagarajan, V. Adsorption studies of NH3 molecules on functionalized germanene nanosheet–a DFT study. *Chemical Physics Letters* **2016**, *665*, 22–30.
- (40) Jamdagni, P.; Kumar, A.; Sharma, M.; Thakur, A.; Ahluwalia, P. Electronic prop-

- erties and STM images of vacancy clusters and chains in functionalized silicene and germanene. *Physica E: Low-dimensional Systems and Nanostructures* **2017**, *85*, 65–73.
- (41) Rezaei, M.; Sisakht, E. T.; Fazileh, F.; Aslani, Z.; Peeters, F. Tight-binding model investigation of the biaxial strain induced topological phase transition in GeCH 3. Physical Review B 2017, 96, 085441.
- (42) Ren, C.-C.; Zhang, S.-F.; Ji, W.-X.; Zhang, C.-W.; Li, P.; Wang, P.-J. Tunable electronic and topological properties of germanene by functional group modification. *Nanomaterials* **2018**, *8*, 145.
- (43) Bianco, E.; Butler, S.; Jiang, S.; Restrepo, O. D.; Windl, W.; Goldberger, J. E. Stability and exfoliation of germanane: a germanium graphane analogue. *ACS nano* **2013**, *7*, 4414–4421.
- (44) Si, C.; Liu, J.; Xu, Y.; Wu, J.; Gu, B.-L.; Duan, W. Functionalized germanene as a prototype of large-gap two-dimensional topological insulators. *Physical Review B* **2014**, 89, 115429.
- (45) Graziosi, P.; Kumarasinghe, C.; Neophytou, N. Impact of the scattering physics on the power factor of complex thermoelectric materials. *Journal of Applied Physics* **2019**, 126.
- (46) Mott, N. F.; Davis, E. A. *Electronic process in non-crystalline materials*; Oxford University Press Oxford, 1971; Vol. 14.
- (47) Allen, P. B. Electron transport. Contemporary Concepts of Condensed Matter Science **2006**, 2, 165–218.
- (48) Sohier, T.; Gibertini, M.; Calandra, M.; Mauri, F.; Marzari, N. Breakdown of optical phonons' splitting in two-dimensional materials. *Nano letters* **2017**, *17*, 3758–3763.

- (49) Zhang, C.; Wang, R.; Mishra, H.; Liu, Y. Two-Dimensional Semiconductors with High Intrinsic Carrier Mobility at Room Temperature. *Physical Review Letters* 2023, 130, 087001.
- (50) Li, J.; He, C.; Meng, L.; Xiao, H.; Tang, C.; Wei, X.; Kim, J.; Kioussis, N.; Malcolm Stocks, G.; Zhong, J. Two-dimensional topological insulators with tunable band gaps: Single-layer HgTe and HgSe. *Scientific reports* **2015**, *5*, 14115.
- (51) Poncé, S.; Margine, E. R.; Verdi, C.; Giustino, F. EPW: Electron-phonon coupling, transport and superconducting properties using maximally localized Wannier functions. Computer Physics Communications 2016, 209, 116–133.
- (52) Li, W. Electrical transport limited by electron-phonon coupling from Boltzmann transport equation: An ab initio study of Si, Al, and MoS 2. *Physical Review B* **2015**, *92*, 075405.
- (53) Ma, J.; Nissimagoudar, A. S.; Li, W. First-principles study of electron and hole mobilities of Si and GaAs. *Physical Review B* **2018**, *97*, 045201.
- (54) Macheda, F.; Bonini, N. Magnetotransport phenomena in p-doped diamond from first principles. *Physical Review B* **2018**, *98*, 201201.

TOC Graphic

